International Journal of Mass Spectrometry 308 (2011) 155–166

Contents lists available at SciVerse ScienceDirect

International Journal of Mass Spectrometry

journal homepage: www.elsevier.com/locate/ijms

Photofragmentation of and electron photodetachment from a GFP model chromophore in a quadrupole ion trap

Matthew W. Forbes, Andrea M. Nagy [1], Rebecca A. Jockusch *

Department of Chemistry, University of Toronto, ON M5S 3H6, Canada

ARTICLE INFO

Article history:
Received 28 February 2011
Received in revised form 9 August 2011
Accepted 16 August 2011
Available online 22 August 2011

Keywords:
Green fluorescent protein chromophore
HBDI
Electron photodetachment
Quadrupole ion trap mass spectrometry
Electronic action spectroscopy
Photodissociation

ABSTRACT

Although green fluorescent protein (GFP) is widely used in the biological sciences, the photophysics controlling GFP fluorescence versus non-radiative decay pathways are not well understood. In previous work (Forbes and Jockusch, J. Am. Chem. Soc. 2009), we reported that a gaseous anionic model chromophore of GFP, *p*-hydroxybenzylidene-2,3-dimethylimidazolone (HBDI$^-$), deactivates via electron photodetachment (*ePD*) as well as photofragmentation. Distinct electronic action spectra were measured for these two pathways upon activation of HBDI$^-$ in a quadrupole ion trap (QIT) mass spectrometer. Here, we explore the mechanisms of HBDI$^-$ dissociation following photoexcitation at two characteristic wavelengths: 410 nm, at which the dominant pathway is *ePD* and at 480 nm, at which the branching ratio between *ePD* and fragmentation depends strongly on the experimental conditions employed. The results indicate that *ePD* from HBDI$^-$ at 410 nm is a single photon process with a rate that is unaffected by changing the pressure of the helium bath gas. This is consistent with a prompt electron detachment process at 410 nm. At 480 nm, photofragmentation in the QIT requires absorption of more than one photon and is suppressed by collisions, while *ePD* results from both single and multiple photon absorption. A model that accounts for all these observations is discussed. *ePD* and effective absorption cross sections are estimated as is the rate of collisional cooling within the QIT. This work explores the connection between absorption and action spectroscopy as applied to the photophysics of a biologically important chromophore.

© 2011 Elsevier B.V. All rights reserved.

1. Introduction

The use of autofluorescent proteins (FPs), of which the best known is the green fluorescent protein (GFP), is now widespread in the biological sciences. FPs are commonly employed as bright fluorescent tags, which can be used to track the location and expression levels of proteins to which they are attached [1]. In native FPs, the light-absorbing and emitting chromophore is stabilized at the center of the barrel-shaped protein [2]. The spectroscopic properties of the chromophore are dependent on both its stabilizing interactions within the protein scaffold [3] and its ionization state [4–7]. Wild-type (wt) GFP exhibits two broad absorption features: the A band (395–397 nm) assigned to the neutral chromophore and the B band (470–475 nm) assigned to the anionic form [4–7]. The B-form of GFP is highly fluorescent, with an emission maximum at $\lambda_{em}^{max} = 504$ nm and quantum yield $\Phi_{fl} = 0.79$ [8].

Very recently, a new role for FPs has been identified, that of light-induced electron transfer agents [9]. This proposal is based on the recently discovered phenomenon in GFPs dubbed "oxidative redding," which is a change from green to red fluorescence occurring when electron acceptors are present in the environment of the FP [9]. Oxidative redding was attributed to the donation of two electrons from the FP chromophore to nearby oxidants [9].

p-Hydroxybenzylidene-2,3-dimethylimidazolinone (HBDI: Scheme 1), is a simple model chromophore for GFP. While the surrounding protein clearly modulates the properties of the chromophore, most famously by increasing the fluorescence quantum yield over 1000-fold [10–14], numerous experimental and computation studies of small model chromophores such as HBDI have provided useful insight into the mechanism and control of FP activity [12,13,15–42]. Electron detachment from the chromophore upon irradiation, a key step in oxidative redding, has also been inferred from pump-probe experiments on HBDI in solution [22,23]; however, electron detachment from solvated HBDI$^-$ required the sequential absorption of two visible photons [22], which would make it a minor deactivation pathway upon photoexcitation.

Abbreviations: *ePD*, electron photodetachment; FP, fluorescent protein; GFP, green fluorescent protein; HBDI, *p*-hydroxybenzylidene-2,3-dimethylimidazolinone; HBI, *p*-hydroxybenzylidene-imidazolinone; QIT, quadrupole ion trap; Ti:Sapph, Titanium Sapphire; wt, wild type.

* Corresponding author. Tel.: +1 416 946 7198; fax: +1 416 978 8775.
E-mail address: rebecca.jockusch@utoronto.ca (R.A. Jockusch).
[1] Present address: Department of Chemistry, University of Konstanz, Germany.

1387-3806/$ – see front matter © 2011 Elsevier B.V. All rights reserved.
doi:10.1016/j.ijms.2011.08.016

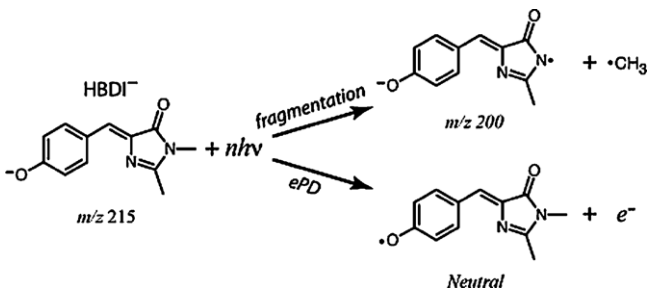

Scheme 1.

Other notable studies of model GFP chromophores include those of Andersen and co-workers, who investigated the electronic absorption characteristics of several *gaseous* chromophores including anionic [29], cationic [30] HBDI and 'neutral' model chromophores [31,33] using a storage ring. Andersen's group showed that the maximum for photofragmentation of $HBDI^-$ in the gas phase (λ_{max} = 479 nm, FWHM = 45 nm) [29] matched closely the absorbance of the B-band of wt-GFP and suggested that the native protein structure provides an electronic environment for the chromophore similar to what it experiences in the gas phase [29].

We have recently reported results from an investigation of the deactivation pathways of gaseous $HBDI^-$ stored and photoactivated in a quadrupole ion trap (QIT) mass spectrometer which has been modified to enable action spectroscopy and laser-induced fluorescence measurements on mass-selected ions [34]. Consistent with the low fluorescence quantum yield observed in solution, no steady-state fluorescence from $HBDI^-$ was observed in the gas phase at ambient temperature (295 K). Rather, the model chromophore undergoes photodissociation readily at low irradiation energies and exhibits two distinct and wavelength-dependent processes shown in Scheme 1: (i) photofragmentation as observed previously by Andersen and coworkers [29] and (ii) electron photodetachment (*ePD*). Distinct action spectra were measured for these two pathways. The electron detachment process gives rise to a broad band in the action spectrum (390–510 nm) having significant vibronic features that are not observed in the fragmentation channels alone, which themselves exhibit an action spectrum that matches closely that measured previously by Andersen and coworkers [29]. The total action spectrum (the sum of *ePD* and fragmentation pathways) measured in the QIT matched well with the low-temperature absorbance spectra of intact GFPs [4,5] and the measured vibronic structure is also well reproduced by computed absorbance spectra from high-level *ab initio* calculations on $HBDI^-$ [43] and on a similar model chromophore (HBI^-) [35]. Nevertheless, the correspondence between a gas-phase action spectrum and linear absorption spectrum can be complicated because the former may reflect the absorption of multiple photons, deactivation dynamics, dissociation threshold and kinetic shift. Very recently, Zenobi and coworkers have suggested that the absorption band maximum of gaseous $HBDI^-$ lies at significantly higher energy than the photofragmentation maximum found in the storage ring and QIT action spectroscopy experiments [44].

Here, we investigate the mechanisms of photofragmentation of and electron photodetachment from HBDI anions, which are stored and activated in a QIT mass spectrometer. Dissociation is explored at two characteristic excitation wavelengths: 410 nm at which *ePD* dominates, and 480 nm at which the product branching ratio in the QIT can be controlled to favor either photofragmentation or *ePD*. The effects of several experimental parameters, including laser power (P), pulse rate (*f*), irradiation time (t) and pressure of helium (He) bath gas (P_{He}) are investigated. We show that photofragmentation of $HBDI^-$ in the QIT requires absorption of more than one photon, that electron detachment at 410 nm results predominantly from the absorption of a single photon and that at 480 nm components of both single- and multiple-photon driven *ePD* are apparent. Cross sections for *ePD* and absorption are estimated and a model that accounts for all experimental observations is discussed.

2. Materials and methods

2.1. Sample preparation

The GFP model chromophore *p-hydroxybenzylidene-2,3-dimethyl-imidazolinone* (HBDI) was provided by Prof. V.M. Dong, C. Yeung and C. Yang (University of Toronto). Briefly, it was prepared using a two step sequence [10,45] from commercially available 4-acetoxybenzaldehyde. Condensation of the aldehyde with *N*-acetylglycine afforded the corresponding azlactone (65%) by the Erlenmeyer azlactone synthesis. Subsequent aminolysis with methylamine and cyclization yielded the desired compound (33%). Solutions of HBDI were prepared at a concentration of ~0.1–1 μM in 1/4 (v/v) H_2O/MeOH and were electrosprayed by infusion at a flow rate of 2 μL min^{-1}.

2.2. Laser setup

The light source used for photodissociation is a *Tsunami* Titanium:Sapphire (Ti:Sapph) laser (Spectra-Physics, Mountain View, CA). The Ti:Sapph crystal is pumped by the second harmonic (532 nm) of a *Millenia Pro 10s* Nd:YVO_4 (Spectra-Physics) and provides tuneable near-IR light in the 700–1080 nm range with output powers ranging from 200 mW to 1.8 W. When mode-locked, the *Tsunami* pulses at a rate of 80 MHz with a pulse duration of 100–130 fs. Typical bandwidths of the mode-locked pulses are in the range 10–20 nm at full-width half-maximum (FWHM). The IR output is frequency doubled using a Type I second harmonic generating crystal of beta-barium borate (Newlight Photonics, Toronto, ON) providing near-UV/visible light in the 350–540 nm range with powers ranging from 20 mW to 400 mW. The laser power is attenuated using an adjustable neutral density filter and monitored with a Solo 2 power meter (Gentec Electro-Optics Inc., Quebec City, QC) equipped with a XLP12-1S-H2 detector (power-noise level ±0.5 μW). The laser powers (P) used for the various experiments are summarized in Table 1

2.3. Pulse picker

To perform photodissociation experiments with pulse rates below the standard 80 MHz repetition rate of the Ti:Sapph laser, frequency division was carried out using a pulse picker (Model 350-160 KD*P Series Modulator, Model 305 Synchronous Countdown and a Model 25D Digital Amplifier) from ConOptics Inc., Danbury, CT. Pulse rates (*f*), number of pulses (N_{pulses}) and the number of photons ($n_{h\nu}$) used for different experiments are summarized in Table 1.

2.4. Quadrupole ion trap mass spectrometry

Gaseous ions were photodissociated in an Esquire 3000+ QIT mass spectrometer (Bruker Daltonik GmbH, Bremen, Germany) that has been modified for spectroscopy and described previously [46,47]. Ions are generated by electrospray ionization (ESI), injected into the QIT and mass-selected. The ion accumulation time is adjusted to obtain the desired ion population as monitored by the ion charge control (*ICC*) value. Following ion isolation, a delay period of at least 50 ms (and typically 125 ms) was implemented using the first MS^2 software event to ensure that the ion ensemble was both spatially and vibrationally cooled. Next, a trigger from the Esquire 3000+ opens a shutter to allow transmission of the

Table 1
Summary of the experimental parameters for the photodissociation of $HBDI^-$.

	Description	Action spectroscopy	Power dependence	Kinetics experiments	Pressure dependence	Pulse rate experiments
ICC	Ion charge control	3×10^4	3×10^4	3×10^4	3×10^4	3×10^4
$\Delta P_{He}/10^{-4}$ mbar	Externally measured Helium pressure	1.07	1.07	0.20–1.23	0.15–0.952	0.34
$P_{He,trap}/10^{-3}$ mbar	Helium pressure in trap	2.16	2.16	0.40–2.47	0.30–1.92	0.69
q_z	QIT trapping parameter	0.25	0.25	0.25	0.25	0.59
λ_{ex}/nm	Excitation wavelength	390–510	410, 480	410, 480	480	410, 480
P/mW	Irradiation power	4.0	0–40.0 (410 nm) 0–8.0 (480 nm)	20.0 (410 nm) 4.0 (480 nm)	4.0	8.8–0.1 (410 nm) 7.5–0.1 (480 nm)
t/ms	Irradiation time	250	250	0–400 (410 nm) 0–500 (480 nm)	50	27–2160
f/MHz	Laser pulse repetition rate	80	80	80	80	40–0.5
Δt/ns	Time between laser pulses	12.5	12.5	12.5	12.5	25–2000
N_{pulses}	Number of laser pulses	20×10^6	20×10^6	$0–40 \times 10^6$	4×10^6	1.1×10^6
$n_{h\nu}$/*irradiation*	Number of photons per irradiation	2.0×10^{15} (390 nm)	$0–2.1 \times 10^{16}$ (410 nm)	$0–1.0 \times 10^{16}$ (410 nm)	4.8×10^{14}	4.9×10^{14}
		2.6×10^{15} (510 nm)	$0–4.8 \times 10^{15}$ (480 nm)	$0–2.4 \times 10^{15}$ (480 nm)		

laser beam in to the QIT. Trapped ions are irradiated during MS^n events (n = 3–11) that are provided within the Esquire Control software and are normally used for collision-induced dissociation. Ion irradiation times (t) used in the experiments are summarized in Table 1. After irradiation, a mass-selective instability scan ejects all ions from the trap in order to produce a mass spectrum. This experimental sequence is generally repeated 50–200 times to minimize effects resulting from fluctuations in the electrospray.

The trapping parameter (q_z) at which ions are stored in the QIT during irradiation influences strongly the irradiation efficiency of the ion cloud; ions stored at higher q_z experience a larger trapping potential that decreases the size of the ion cloud and hence improves the intersection of the laser beam with the ion cloud at the center of the trap [46,47]. However, higher q_z values during ion irradiation also increase the low-mass cutoff (LMCO) of the QIT [48], precluding storage and detection of low m/z fragment ions. For the experiments reported here (with the exception of the pulse rate dependence), a q_z value of 0.25 was used in order to permit mass analysis of all the significant product ions.

The QIT is operated with a significant pressure of He bath gas, which dramatically affects the rate of photofragmentation of stored ions at a given laser power and irradiation time (see Section 3). The added pressure of helium (ΔP_{He}) above the base pressure is measured externally to the ion-trapping region using a Granville-Phillips ionization gauge (Brooks Automation, Chelmsford, MA). As previously reported [46], we have computed the conductance of gas flow from the quadrupole ion trap assembly ($\sim$2.5 L s^{-1}) to estimate the He pressure inside the QIT electrode assembly ($P_{He,trap}$). The externally measured range of added pressures translates, after corrections for gas-flow and sensitivity of the gauge to helium, to estimated internal pressures of 0.30–2.47 $\times 10^{-3}$ mbar (0.22–1.85 mTorr). The measured added pressure of He and the computed pressures within the trap are summarized in Table 1.

The hardsphere collision rate (z_{12}) of the trapped precursor ions with helium bath gas was calculated according to Eq. (1) where k_B is Boltzmann's constant, ρ_{He} is the number density of He, μ is the reduced mass and an estimated collision cross-section of $HBDI^-$ (σ_{12}) of 80 Å^2 is used.

$$z_{12} = \sigma_{12}\sqrt{\frac{8k_BT}{\pi\mu}}\rho_{He} \quad (1)$$

For the range of pressures here, the calculated collision rate is in the range 7400–62,000 s^{-1} or approximately one collision every 135–16 μs. We note that the actual collision rate of the $HBDI^-$ may be somewhat higher than computed with this simple model because the ions are accelerated to higher than thermal kinetic energy in the trap.

2.5. Photodissociation yield calculations

The normalized precursor ion intensity remaining after irradiation ($Y_p = Y_{HBDI^-}$) was computed according to Eq. (2), where I_p^{On} and I_p^{Off} are the intensities of the precursor ion with the laser on and off, respectively. The photodissociation action yield (Y_A) corresponds to the depletion of the precursor ion intensity and is computed according to Eq. (3). For all experiments, the photodissociation mass spectra (laser on) are bracketed by control mass spectra (laser off). I_p^{Off} is taken as the mean intensity of the precursor ion in the control mass spectra recorded before and after ion irradiation. The photodissociation and control mass spectra are recorded with identical experimental sequences (i.e., accumulation and storage times, and q_z) with the exception that the shutter is closed for the control spectra (laser off).

$$Y_p = \frac{I_p^{On}}{I_p^{Off}} \quad (2)$$

$$Y_A = 1 - Y_p \quad (3)$$

The yield of fragment ions (Y_f) is taken as the sum of fragment ion intensities normalized to I_P^{Off}, as shown in Eq. (4), where $I_{f(i)}^{On}$ is the intensity of a given fragment ion (i). The yield due to electron detachment (Y_{ePD}) is inferred from the difference between the intensity of the precursor ion (laser off) and the combined intensities of the precursor and products ions (laser on), given by Eq. (5). Mass discrimination effects, which would complicate determination of the (inferred) *ePD* yield are believed to be negligible in this experiment as, in a concurrent investigation of protonated HBDI (which does not undergo *ePD*), 98% of the parent ion intensity was recovered upon photodissociation [34].

$$Y_f = \frac{\sum_{i=1}^{n} I_{f(i)}^{On}}{I_p^{Off}} \quad (4)$$

$$Y_{ePD} = \frac{I_p^{Off} - I_p^{On} - \sum_{i=1}^{n} I_{f(i)}^{On}}{I_p^{Off}} = Y_A - Y_f \quad (5)$$

Breakdown curves are constructed by plotting the photodissociation yield of $HBDI^-$, fragment ions and electron photodetachment as a function of laser power, irradiation time, He pressure, q_z and

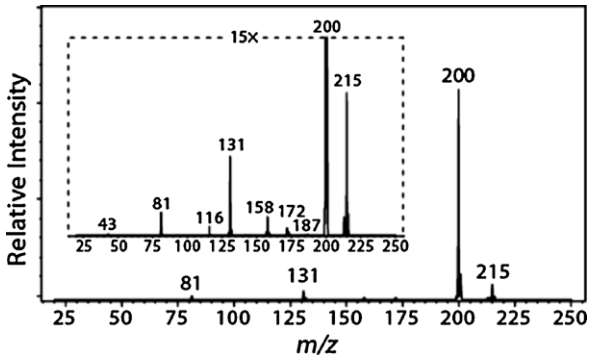

Fig. 1. Photodissociation mass spectrum for $HBDI^-$ (m/z 215) using 480 nm light (P = 20 mW, t = 150 ms, f = 80 MHz, q_z = 0.11, $P_{He,trap} = 0.35 \times 10^{-3}$ mbar). The low-mass cutoff (LMCO) was 26 m/z. The predominant fragment ion is at m/z 200. The inset (15× expansion) shows several other minor fragment ions.

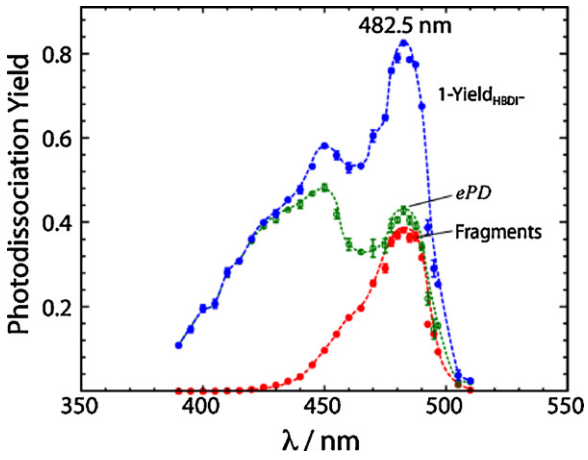

Fig. 2. Photodissociation action spectra of gaseous $HBDI^-$ measured in a quadrupole ion trap showing the decrease in yield of $HBDI^-$ (closed blue circles) with the measured yield from fragmentation channels (closed red circles) and the inferred yield due to electron photodetachment (open green circles). (For interpretation of the references to color in this figure legend, the reader is referred to the web version of the article.)

laser pulse rate. Error bars shown correspond to the standard deviation from triplicate sets of measurements. The (pseudo) 1st-order unimolecular dissociation rate constant (k_{diss}) is obtained from the slope of a plot of $\ln(Y_{HBDI^-})$ versus irradiation time.

3. Results

3.1. Photodissociation pathways

Fig. 1 shows a photodissociation mass spectrum of gaseous $HBDI^-$, stored and irradiated with 480 nm light in the QIT. The dominant fragment ion (m/z 200) arises from a loss of methyl (Scheme 1, pathway (i)) and accounts for ~98% of the fragment ion yield, with additional minor contributions from m/z 187, 172, 158, 131 and 81. These are the same fragment ions observed following multiple collision-induced dissociation in the QIT. However, as we have shown previously [34], the total ion current from precursor + product ions *following* photodissociation is significantly lower than the precursor ion current *prior* to irradiation. This loss of ion current is attributed to electron detachment (Scheme 1, pathway (ii)), the occurrence of which upon was recently verified by Zenobi and coworkers [44]. Action spectra for each pathway, constructed by monitoring the measured photo-fragmentation yield (Y_f) and electron detachment yield (Y_{ePD}) as a function of excitation wavelength, are shown in Fig. 2 as the red and green symbols, respectively. The two pathways clearly have differing wavelength dependencies. Electron detachment occurs over the entire range of irradiation wavelengths used (390–510 nm) and at wavelengths shorter than 425 nm is the dominant dissociation pathway. In contrast, an appreciable yield of fragment ions is observed only in a narrower band at lower photon energies (445–510 nm). Also shown in Fig. 2 is the total action spectrum in blue, which represents the loss of the $HBDI^-$ precursor ion as a function of excitation wavelength.

The measured action spectra reflect the wavelength dependence of $HBDI^-$ absorption; however, measured band intensities depend on dissociation as well as excitation efficiencies. This means that the gas-phase action spectrum is not identical to a linear absorption spectrum; rather, its appearance depends on the experimental conditions used. This dependence can be exploited to investigate the mechanisms of electron detachment and photofragmentation of $HBDI^-$ in the QIT. The dominance of the *ePD* channel at higher photon energies provides the opportunity to examine the electron detachment process independently from the fragmentation channels. In the following sections, we explore the affect of several experimental parameters on *ePD* yield following 410 nm excitation. These results are compared with those from similar experiments using lower photon energy (480 nm), which is near the photodissociation maximum (482.5 nm) observed in the action spectrum.

3.2. Power dependence

Fig. 3 shows photodissociation breakdown plots for $HBDI^-$ as a function of laser power at (a) 410 nm and (b) 480 nm under the same conditions of irradiation time, pulse rate, trapping parameter and He pressure as used to construct the action spectra shown in Fig. 2. Several significant differences are evident. At 410 nm, 250 ms of 40 mW irradiation power results in ~95% disappearance of the $HBDI^-$. Electron detachment is the dominant dissociation mechanism at this wavelength, with the combined appearance of fragment ions comprising <2.5% of the total photodissociation yield. In contrast, with irradiation at 480 nm, the dissociation of $HBDI^-$ is essentially complete after 250 ms with a laser power of just 8 mW. Both electron detachment and fragmentation are significant dissociation channels at this wavelength. At both 410 nm and 480 nm, lower laser powers favor electron detachment and at 480 nm the fragmentation yield clearly depends more strongly on laser power than does *ePD*.

The lower panels in Fig. 3 show semi-logarithmic plots of the remaining $HBDI^-$ yield as a function of irradiation power, which highlights the difference in photodissociation behavior at these two photon energies. The excellent linear relationship with zero-intercept shown in Fig. 3c indicates that the photodissociation measured using 410 nm light, which is essentially all *ePD*, is dominated by a single-photon process. The 410 nm photon energy (3.0 eV) exceeds the computed electron detachment energy (2.4–2.8 eV) [34,40] and so the observed single-photon behavior is consistent with direct detachment of electrons; however, the shortest irradiation time accessible with our apparatus is ~10 ms and is normally much longer (e.g. t = 250 ms). Therefore, these experiments alone do not provide temporal resolution capable of distinguishing between direct photodetachment (fs–ps time frame) and delayed/statistical detachment (ns–ms time frame) [49–51].

In contrast to the simple linear power dependence measured upon irradiation at 410 nm, photodissociation of $HBDI^-$ using 480 nm light (2.6 eV) clearly shows a more complex dependence on laser power (Fig. 3d). The data indicate that photodissociation of $HBDI^-$ under the experimental conditions employed involves the absorption of multiple 480 nm photons. The inset to Fig. 3(d) shows

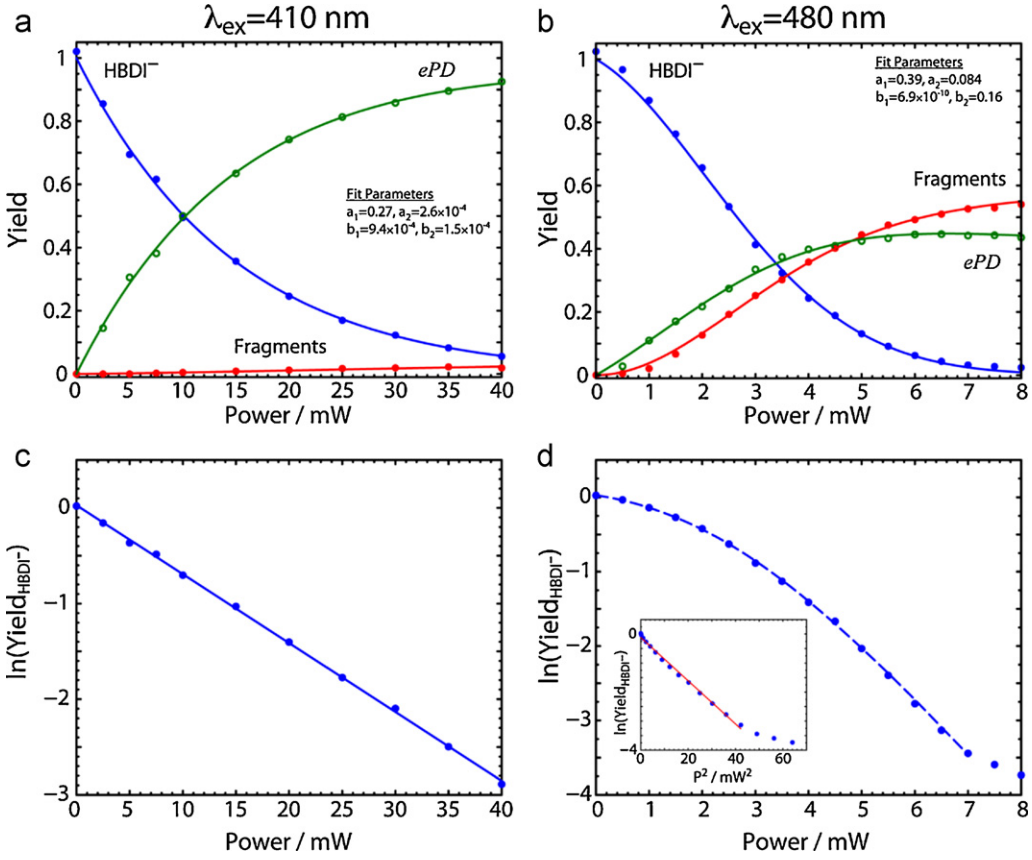

Fig. 3. Power dependence of $HBDI^-$ photodissociation at 410 nm (left side) and 480 nm (right side): (a and b) breakdown curves showing the yield of $HBDI^-$ (blue), fragment ions (red) and electron photodetachment (green) as a function of laser power; (c and d) plots of $\ln(\text{Yield}_{HBDI^-})$ with respect to laser power. The inset in panel (d) shows the dependence of $\ln(\text{Yield}_{HBDI^-})$ on the square of the laser power. Lines show fits to the data as described in Eqs. (6)–(10). (For interpretation of the references to color in this figure legend, the reader is referred to the web version of the article.)

that the data do not fit a simple P^2 dependence. Fitting this data instead with a second order polynomial in power (dotted blue line in Fig. 3d) yields a better result (see Section 4). Power-dependence plots at four different pressures of He (see Figs. S1–S4 in the Supplementary Information) exhibit similar relationships with laser power. Thus, these data suggest that depletion of the precursor ion with 480 nm light is driven by both one- and multiple-photon processes in the QIT.

3.3. Kinetics and pressure dependence

The dissociation kinetics of $HBDI^-$ were investigated as a function of He pressure to determine the effect of collisional relaxation on product yields. Fig. 4(a) and (d) shows kinetic plots for the dissociation of $HBDI^-$ at four different He pressures with irradiation at 410 nm and 480 nm, respectively. The dissociation kinetics at both irradiation wavelengths show excellent pseudo 1st-order behavior. The kinetic plots measured with 410 nm photodissociation have zero-intercepts, while a short induction period is apparent in the 480 nm data measured at lower pressures. Dissociation rate constants (k_{diss}) taken from the slope of the plots of $\ln(\text{Yield}_{HBDI^-})$ versus time are summarized in Table 2.

The 410 nm photodissociation kinetics are insensitive to changing pressure (Fig. 4(a)–(c)). At the three highest pressures, the extracted rate constants are essentially unchanged within the statistical variation of the measurements. At the lowest pressure used (0.40×10^{-3} mbar), the rate of dissociation is increased by approximately 10%. The two accompanying plots (Fig. 4(b and c)) show separately the yield due to fragmentation and electron detachment, respectively, at each pressure. *ePD* yields at 410 nm do not depend noticeably on the He pressure (Fig. 4c), while the small fragmentation yield is increased at the lowest He pressure (Fig. 4b), which explains the increased dissociation rate. These data indicate that collisions suppress fragmentation but have a negligible effect on electron detachment rates at 410 nm. With longer irradiation times (>250 ms), the yield of m/z 200 declines slightly. This is due to photodissociation of the m/z 200 product ion population by 410 nm light and has been confirmed with MS^3 photodissociation experiments (data not shown).

Fig. 4(d) compares kinetic plots for the photodissociation of $HBDI^-$ with irradiation at 480 nm measured at four pressures. After a brief induction period, the data are well fit by first-order kinetics. There is an approximately five-fold increase in the dissociation rate constant as $P_{He,trap}$ is decreased approximately six-fold (Table 2), indicating that collisions suppress photodissociation at this wavelength. The extent of fragment ion formation is highly sensitive to the rate of collisional cooling (Fig. 4(e)) but the yields due to electron detachment appear to follow a single trend (Fig. 4(f)). This

Table 2
Dissociation rate constants (k_{diss}) and statistical variation (s_b) from the univariate regression models fit to the experimental data in Fig. 4(a and d) at four different pressures of He bath gas.

$P_{He,trap}$/mbar	λ = 410 nm (P = 20.0 mW) $k_{diss} \pm s_b/s^{-1}$	λ = 480 nm (P = 4.0 mW) $k_{diss} \pm s_b/s^{-1}$
0.40×10^{-3}	7.1 ± 0.07	24.0 ± 0.6
1.46×10^{-3}	6.3 ± 0.08	9.7 ± 0.2
2.16×10^{-3}	6.4 ± 0.10	5.7 ± 0.1
2.47×10^{-3}	6.5 ± 0.10	5.0 ± 0.1

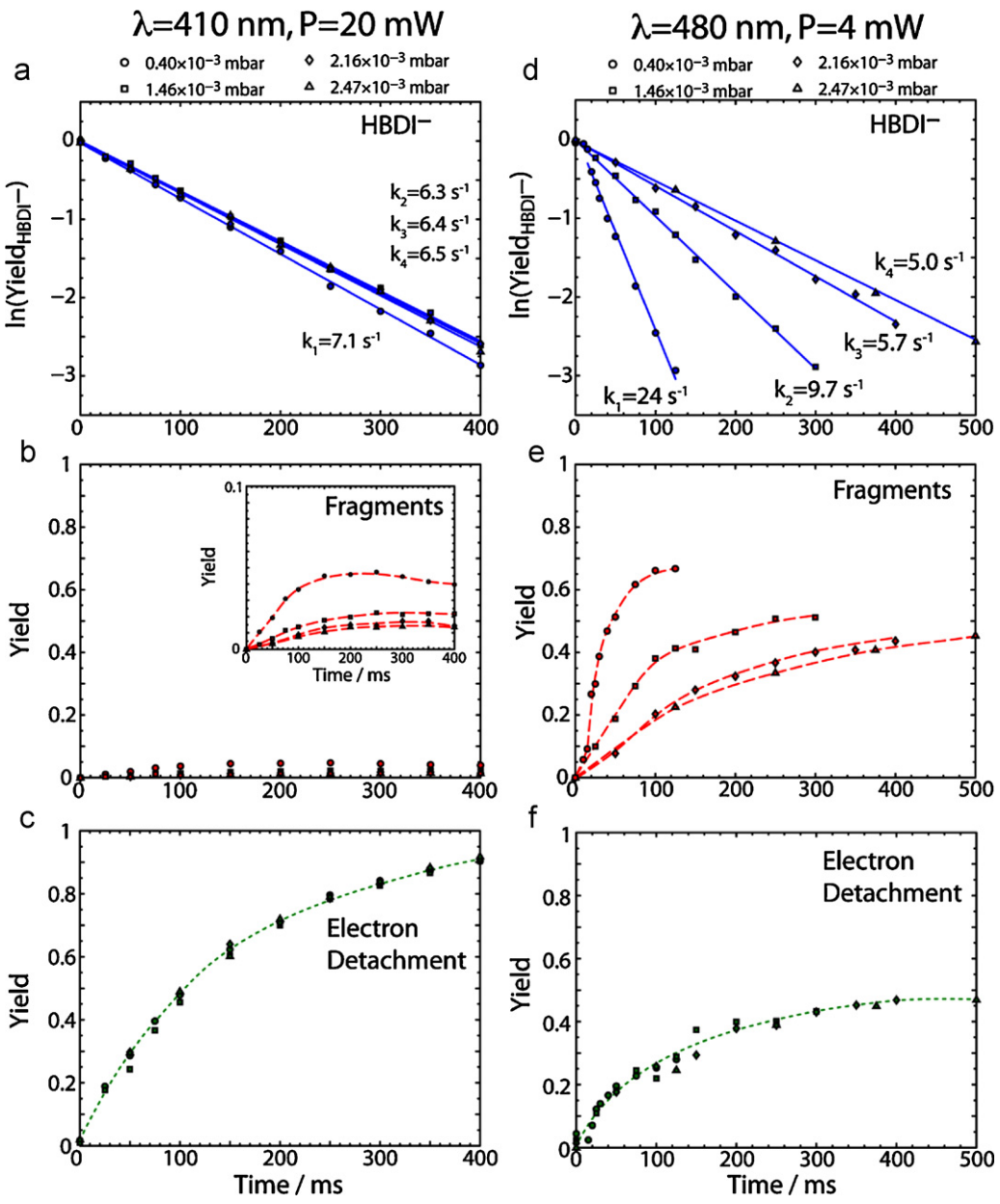

Fig. 4. Photodissociation kinetics of $HBDI^-$ with irradiation with 20 mW of 410 nm light (left side) and 4 mW of 480 nm light (right side) at four different pressures of He bath gas. Top: (a and d) the time dependence of $\ln(\text{Yield}_{HBDI^-})$, showing fits to first-order kinetics; the rate constants ($k_1 - k_4$) measured at each He pressure are noted on the figure. Below: plots showing fragment ion yield (b and e) and electron detachment yield (c and f) as a function of irradiation time at each pressure.

suggests that the rate of electron detachment upon 480 nm excitation, is essentially independent of the rate of collisional cooling, although there is noticeably larger scatter amongst the 480 nm data than the 410 nm data, particularly at shorter irradiation times.

An additional series of measurements was made to further investigate the effect of pressure on the branching ratio at $\lambda_{ex} = 480$ nm under conditions of fixed power (4 mW) and irradiation time (50 ms) (Fig. 5). As the pressure is increased, more $HBDI^-$ precursor survives 50 ms irradiation at this modest laser power. The increase in Y_{HBDI^-} is reflected by an (nearly) equivalent decrease in fragment ion yield. The electron detachment yield shows a slight, yet significant decrease (−0.05 or 36% of the *ePD* yield) as the pressure is increased more than 6-fold. This result indicates that electron detachment at 480 nm is not entirely independent of the He pressure but that the influence is small.

Fig. 5(b) shows a Stern–Volmer plot constructed according to the methods outlined by Dunbar and Fu [52] based on a simple two-photon model for dissociation in a high pressure/low irradiation regime (see Section 4). An acceptable fit to the univariate linear regression model is found with slope of $7.8 \pm 0.4 \times 10^{-14}$ cm^3 molecule^{-1} and intercept of 0.47 ± 0.12. Using this model, an effective absorption cross-section of $(1.3 \pm 0.4) \times 10^{-16}$ cm^2 and collisional cooling rate constant (k_{cool}) of $(2.8 \pm 1.6) \times 10^{-11}$ cm^3 molecule^{-1} s^{-1} are calculated. More detailed considerations of the relative absorption cross-sections and rates of collisional cooling will follow in Section 4.

3.4. Laser pulse rate

A useful method to probe the time-frame of ion activation is by variation of the laser pulse repetition rate [53–55]. Fig. 6 shows the effect of varying the laser pulse repetition rate on the photodissociation of $HBDI^-$. At each pulse rate, the total number of pulses (N_{pulses}) is fixed at 1.1×10^6 and the number of

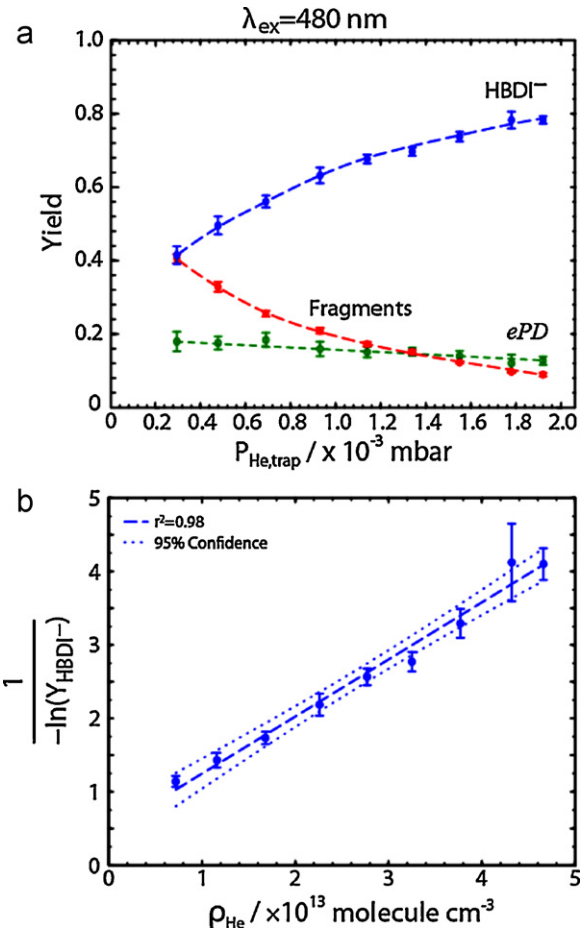

Fig. 5. (a) Remaining yield of $HBDI^-$ (blue), fragment ion yield (red) and electron photodetachment yield (green) as a function of He pressure with 4 mW irradiation at 480 nm. (b) A Stern–Volmer plot showing $-1/\ln(\text{Yield}_{HBDI^-})$ versus number density of He (ρ_{He}). (For interpretation of the references to color in this figure legend, the reader is referred to the web version of the article.)

photons per pulse is also held constant (see Table 1); thus, as the frequency of pulses is decreased, the total irradiation time is increased proportionally to compensate. For example, at 40 MHz the time between pulses (Δt) is 25 ns and the total irradiation time used was 27 ms. At 4 MHz, the irradiation time was increased to 270 ms to deliver 1.1 million pulses. To account for the difference in photon energy between 410 nm and 480 nm, the laser pulse energy was adjusted appropriately (see Table 1) to provide the same number of photons (4.9×10^{14}) at both excitation wavelengths. Note that the laser pulse repetition rate does not provide a direct measure of the time between absorption events because the pulse energy (200–230 pJ $pulse^{-1}$ or 4.5×10^8 photons $pulse^{-1}$) is extremely low, so an average ion in the ensemble does not absorb a photon with each pulse. Rather, the pulse rate experiments probe the competition between collisional cooling of activated molecules and the probability of photon absorption from multiple pulses. The estimated collision frequency at the pressure used is one collision per 60 μs, much lower than the laser pulse repetition rate. This corresponds to an average of 2300 pulses between collisions at 40 MHz and 30 pulses between collisions at 500 kHz pulse repetition rates.

Fig. 6 shows the effect of changing the delay between laser pulses on the dissociation yield of $HBDI^-$ at the two characteristic excitation wavelengths, 410 nm and 480 nm. With irradiation at 410 nm (Fig. 6a), the photodissociation yield of $HBDI^-$ and the branching ratio between electron detachment and fragmentation is largely unaffected by the time delay between pulses. A very small contribution (<1%) from the fragmentation channel is observed at the highest pulse rate ($\Delta t = 25$ ns) but declines rapidly to zero above $\Delta t = 200$ ns (Fig. 6a, inset).

In contrast, Fig. 6b illustrates that photodissociation of $HBDI^-$ at 480 nm is dramatically affected by the time-delay between laser pulses. Upon irradiation with the same number of photons as at 410 nm, there is nearly complete dissociation of the precursor ion when the time between pulses is short. However, as the time between pulses is increased, there is a sharp increase in the yield of precursor ions remaining following the irradiation period; Y_{HBDI^-} reaches ~0.8 for $\Delta t = 600$ ns. With a longer time between pulses, Y_{HBDI^-} continues to increase but at a much slower rate. The branching ratio between fragmentation and electron detachment at $\lambda_{ex} = 480$ nm is also sensitive to the laser pulse rate. Fragmentation is favored over electron detachment at higher pulse rates (branching ratio ~3:2 for $\Delta t = 25$ ns). The yield of *both* fragmentation and *ePD* decrease with longer pulse delays; however, the fragmentation channel is clearly more sensitive to pulse rate than *ePD*. Y_f is nearly completely suppressed with long Δt ($Y_f \approx 2\%$ at $\Delta t = 1800$ ns) while Y_{ePD} remains near 10%. The change in branching ratio indicates that the number of photons involved with fragmentation is higher than for *ePD*. It is interesting to note that electron detachment yield also

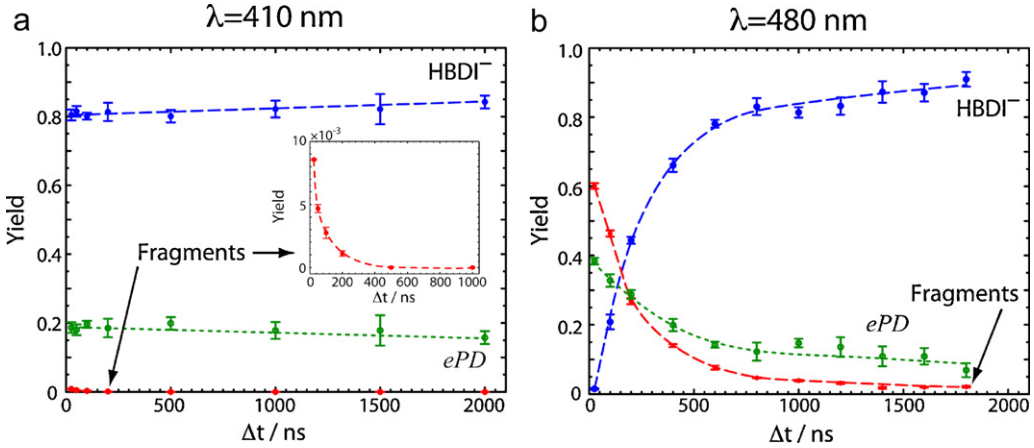

Fig. 6. The effect of laser pulse repetition rate on the yield of $HBDI^-$ precursor ion (blue), fragment ions (red) and electron detachment product (green). Yields are plotted at (a) 410 nm and (b) 480 nm as a function the time between pulses (Δt), which is proportional to the overall irradiation time (t) and inversely proportional to the pulse repetition rate. Each point in both plots was obtained using the same number of photons from the excitation laser ($n_{h\nu} = 4.9 \times 10^{14}$). (For interpretation of the references to color in this figure legend, the reader is referred to the web version of the article.)

declines significantly between Δt = 25 ns and 600 ns. This indicates that some of the *ePD* occurring at shorter time delays is due to the absorption of more than one photon.

Note that the data shown in Fig. 6 illustrate clearly that the fragmentation observed is due to the absorption of photons from multiple pulses (multiple photon dissociation) rather than the absorption of more than one photon within the same laser pulse (multi-photon dissociation). If multi-photon dissociation were the dominant process, the extent of fragmentation should have remained constant, because the pulse characteristics (duration and photons per pulse) are held constant in this experiment as is the pressure-dependent cooling rate. What does change in this experiment is the amount of cooling because the number of collisions experienced by an ion increases linearly with Δt. The fact that the fragment ion signal decays to almost zero at long pulse delays indicates that the photofragmentation is due to a slow activation process, i.e., multiple photon dissociation.

The pulse rate experiments can be viewed as an alternative way to investigate the power dependence of photodissociation. The lowest pulse rate used corresponds to 100 μW, somewhat lower than the lowest power used in the power dependence studies shown in Fig. 3. Plots of the dissociation rate constants derived from the pulse rate data (analysis not shown) exhibit the same power relationship as those shown in Fig. 3.

4. Discussion

The dynamics of photodissociation in the quadrupole ion trap are complex due to the combined and/or entwined effects of several experimental parameters that affect the relative rates of ion activation and deactivation including irradiation power, wavelength, pulse repetition rate, the irradiation efficiency of the ion cloud (dependent on q_z and the size of the laser beam) and the rate of collisional cooling (dependent on $P_{He,trap}$). Thus, the choice of experimental conditions may dramatically affect the appearance of action spectra, which measure the consequence of absorption (here, photofragmentation or electron photodetachment) and thus do not provide a direct measure of the absorption cross section. To understand better the connection between the measured action spectra, dissociation pathways and absorption, we explore below more fully the dynamics of ion activation and deactivation. We start with a brief review of the results, then describe a model that accounts for the experimental observations. Finally, simplified models are used to estimate quantities including reaction cross sections and collisional cooling rates.

Electron detachment is the dominant dissociation mechanism for $HBDI^-$ in the quadrupole ion trap upon activation at 410 nm, under all experimental conditions investigated in this work. The detachment yield dependence on power (Fig. 3), pressure (Fig. 4) and pulse rate (Fig. 6) indicate that the *ePD* results from absorption of a single 410 nm (3.0 eV) photon. Under conditions of high laser power and/or low pressure, a minor contribution from fragmentation is observed, indicating that fragmentation requires the absorption of more than one 410 nm photon.

The photodissociation of $HBDI^-$ using 480 nm light shows significantly more complex behavior than was observed at 410 nm. Taken together, the dependence of Y_{ePD} and Y_f at 480 nm upon power (Fig. 3), pressure (Figs. 4 and 5) and pulse rate (Fig. 6) indicate that fragmentation results from the absorption of multiple photons and can be suppressed by collisions. The behavior of the electron detachment channel shows a much smaller dependence on pressure (Fig. 5) and photon delivery rate (Fig. 6). At this photon energy (2.6 eV), it appears that *ePD* arises from both one- and two-photon absorption. The existence of multiple-photon dissociation for $HBDI^-$ has been mentioned previously in reports from our laboratory [34,56] as well as in a recent report from the Zenobi laboratory [44].

While the results presented here indicate that both one- and two photon processes contribute significantly to the observed photodissociation of $HBDI^-$ in the quadrupole ion trap, photodissociation studies of $HBDI^-$ at ELISA have shown that photodissociation proceeds primarily by absorption of a single photon at low pressure (10^{-11} mbar) [32]. The differing power dependencies observed in the storage ring and QIT experiments can be rationalized as follows. Time-resolved measurements following irradiation with a single, nanosecond laser pulse in the storage ring experiments show that the unimolecular fragmentation is relatively slow and rates are well described by an Arrhenius-type thermal activation model; the extracted decay rates correspond to ~28–450 μs lifetimes upon excitation between 450 and 500 nm [32]. These lifetimes are somewhat longer than the collisional time-scales at the elevated pressures used in the QIT. A single, or a small number of collisions, removes enough energy that single-photon fragmentation is suppressed on the time scale of the QIT experiments. The absorption of multiple photons is required to increase ion internal energy sufficiently to achieve fragmentation rates that effectively out-compete collisional cooling in the QIT.

4.1. Photodissociation models

Scheme 2 shows a model that accounts for the appearance of both single- and two-photon dissociation products of $HBDI^-$ in the QIT. The precursor ion population ($HBDI^-$), which has an absorption cross-section σ_1, is irradiated with an effective photon irradiance (φ, see below). Absorption of a photon creates an electronic excited state ($HBDI^{-\dagger}$) that can lead either to detachment of an electron with rate constant k'_{ePD}, or internal conversion and intramolecular vibrational redistribution (IVR). Following IVR, a vibrationally excited intermediate ($HBDI^{-*}$) remains. The warm intermediate suffers collisions with helium bath gas that remove internal energy at a rate that is proportional to the collisional cooling rate constant and the pressure. If the rate of collisional cooling is not too high, absorption of a second photon by the warm intermediate (with absorption cross section σ_2) further elevates the ion to a state $HBDI^{-\dagger *}$ from which either electron detachment (with rate constant k''_{ePD}) or IVR can occur thus producing a hot intermediate, $HBDI^{-**}$. $HBDI^{-**}$ may subsequently fragment (rate constant k''_{frag}) or be cooled by further collisions with the bath gas. The fact that single photon *ePD* is the dominant process upon excitation at 410 nm is explained by the rate of electron detachment being substantially faster than IVR at this energy. The relative decrease in electron detachment yield and substantial increase in fragment ion yield upon excitation at 480 nm can be explained by a decrease in k'_{ePD} upon excitation at 480 nm (2.6 eV) compared to 410 nm (3.0 eV), meaning that *ePD* does not compete as effectively with IVR at the lower energy. An increase in pressure results in increased collisional cooling, suppressing multiple photon *ePD* and fragmentation. Unfortunately, we have not been able to solve the rate equations from this model so far, so a simplified kinetic model was used.

Our simplified kinetic model allows for both single- and two-photon dissociation, but neglects explicit consideration of collisional cooling. The equations for product ion formation and remaining precursor ion abundance in this simplified model are given by Eqs. (6)–(8).

$$Y_{ePD} = \frac{k_{ePD}}{k_{frag} + k_{ePD}} [1 - e^{-(k_{frag}+k_{ePD})t}] \quad (6)$$

$$Y_f = \frac{k_{frag}}{k_{frag} + k_{ePD}} [1 - e^{-(k_{frag}+k_{ePD})t}] \quad (7)$$

Table 3
Summary of the fitting parameters obtained from the laser power-dependence experiments. The standard error of the fit (s_e) is also indicated.

λ_{ex}/nm	$P_{He,trap}$/mbar	k_{ePD}		k_{frag}		
		a_1	a_2	b_1	b_2	s_e
410	2.16×10^{-3}	0.27	2.6×10^{-4}	9.4×10^{-4}	1.5×10^{-4}	0.014
480	1.46×10^{-3}	0.33	0.14	1.2×10^{-9}	0.27	0.021
480	1.81×10^{-3}	0.23	0.14	3.2×10^{-9}	0.21	0.029
480	2.16×10^{-3}	0.39	0.084	6.9×10^{-10}	0.16	0.014
480	2.47×10^{-3}	0.38	0.078	5.1×10^{-10}	0.14	0.026

$$Y_{HBDI^-} = 1 - (Y_{ePD} + Y_f) \quad (8)$$

Note that the ratio of rate constants in Eqs. (6) and (7) results from the *ePD*/fragmentation branching ratio while the term in brackets represents the total precursor ion population, which decays exponentially in time with a rate constant of $k_{frag} + k_{ePD}$. k_{frag} and k_{ePD} were each written as 2nd order polynomials of power, to allow for both single photon and two photon dependence, as shown in Eqs. (9) and (10).

$$k_{ePD} = a_1 P + a_2 P^2 \quad (9)$$

$$k_{frag} = b_1 P + b_2 P^2 \quad (10)$$

The 410 and 480 nm power dependence data at multiple pressures (Fig. 3 and Figs. S1–S4) were separately fit with this simplified model. The results are summarized in Table 3. In each data set, the fit identifies a significant component of single-photon electron detachment indicated by the a_1 parameter, which ranges from 0.23 to 0.39. There are also significant components of two-photon electron detachment identified at λ_{ex} = 480 nm (a_2 = 0.078–0.14) which is consistent with the observations from the pressure- and pulse-rate dependence. The fits reinforce the conclusion that any contribution from two-photon electron detachment at λ_{ex} = 410 nm is negligible ($a_2 = 2.6 \times 10^{-4}$). Finally, it is noteworthy that the values for the b_1 parameter are all essentially zero, indicating that photofragmentation within the quadrupole ion trap requires the absorption of at least two (and possibly more) photons.

4.2. Electron detachment cross-section with λ_{ex} = 410 nm

The reaction for single-photon electron detachment is shown in Eq. (11), where σ_{ePD} is the electron detachment cross section and φ is the effective photon irradiance (photons per second per area). φ can be calculated from Eq. (12), in which $n_{h\nu}$ is the number of photons, t is the irradiation time, A is the cross section of the excitation laser beam (which has an $1/e^2$ diameter of 620 μm from knife edge measurements), and θ is the fractional overlap of the ion cloud and laser beam. The latter accounts for the fact that the ion cloud is larger than the laser beam, so a given ion travels in and out of the laser beam path during the irradiation period, resulting in its being exposed to fewer photons than it would be if the entire ion cloud were within the laser beam's path. The overlap is estimated from ion trajectory calculations [47] to be 0.25 for q_z = 0.25 and 0.65 for q_z = 0.59. When single-photon *ePD* is the only dissociation process that occurs, k_{diss} is related to the electron detachment cross-section (σ_{ePD}) as shown in Eq. (13).

$$HBDI^- \xrightarrow{\sigma_{ePD}\varphi} HBDI^\bullet + e^- \quad (11)$$

$$\varphi = \frac{n_{h\nu}\theta}{tA} \quad (12)$$

$$\sigma_{ePD} = \frac{k_{diss}}{\varphi} = \frac{k_{diss} tA}{n_{h\nu}\theta} \quad (13)$$

Taking the dissociation rate constant from the kinetics (Table 2) at 410 nm returns a value for the electron detachment cross section of $HBDI^-$ of 1.9×10^{-18} cm^2. Electron detachment cross-sections upon excitation at 410 nm have been extracted from several data sets and are reasonably self-consistent, ranging from 1.6×10^{-18} cm^2 from the power dependence data (Fig. 3) to 1.9×10^{-18} cm^2 from the kinetics, action spectrum (Fig. 2) and pulse rate data (Fig. 6). These values seem reasonable, given that 410 nm is well off the excitation maximum and keeping in mind that the single-photon electron detachment cross section is equal to the product of absorption cross section and quantum yield for electron detachment (see below). The equivalent molar *ePD* cross-section is ~1100 M^{-1} cm^{-1}. We estimate that the uncertainty in the absolute *ePD* cross-section determined here is in the range of ±50%, a value which reflects primarily uncertainties in the fractional overlap between the laser beam and ion cloud.

The quantum yield for electron detachment (fraction of photoexcited $HBDI^-$ from which electrons detach) must be less than one, otherwise no multiple photon processes could occur. In fact, the small fragmentation yield observed at high power (Fig. 3a) and high pulse rate (Fig. 6a) and faster kinetics measured at low pressure (Fig. 4a) all point to the possibility of multiple photon processes. From the pulse rate data at 410 nm (Fig. 6a), an upper limit for the quantum yield of electron detachment at this wavelength can be estimated by comparing the limiting *ePD* yield of ~0.15 at slow pulse rates, which is presumably due to single photon absorption, and the *ePD* and fragmentation yields of ~0.18 and 0.01 at high pulse rates. Thus, an upper limit for the *ePD* quantum yield is estimated to be 0.15/0.19 = 0.79.

4.3. Absorption cross-section at λ_{ex} = 480 nm and collisional cooling

Dunbar and Fu [52] showed previously the complete kinetic solution to a sequential two-photon model proposed by Freiser

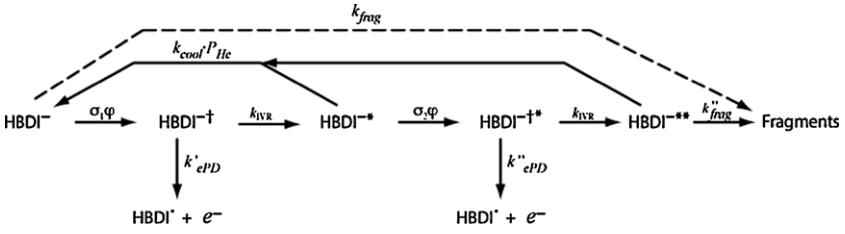

Scheme 2. Photodissociation mechanism of $HBDI^-$ considering one- and two-photon processes.

and Beauchamp [57]. The model assumes that dissociation occurs only following absorption of two photons and that cooling by "strong" (completely deactivating) collisions is the dominant mode of non-dissociative ion deactivation. The precursor ion depletion is described by Eq. (14), in which φ is the effective irradiance (Eq. (12)), k_{cool} is the effective bimolecular rate constant for collisional quenching, ρ_{He} is the number density of the collision gas, t is the irradiation time and σ_1 and σ_2 are the effective absorption cross-sections for the first and second photons, respectively. Imposing the additional assumption that $\sigma_1 = \sigma_2 \equiv \sigma_{480}$ allows further simplification. Written in linear form, this becomes Eq. (15).

$$\frac{1}{-\ln(Y_P)} = \frac{\varphi\sigma_1 + \varphi\sigma_2 + k_{cool}\rho_{He}}{\varphi^2\sigma_1\sigma_2 t} \quad (14)$$

$$\frac{1}{-\ln(Y_P)} = \frac{2}{\varphi\sigma_{480} t} + \frac{k_{cool}}{\varphi^2\sigma_{480}^2 t}\rho_{He} \quad (15)$$

Eq. (15) indicates that a plot of $-1/\ln(Y_p)$ versus pressure (a Stern–Volmer plot) will be linear and that values of k_{cool} and σ_{480} can be determined from the slope and intercept of the plot since φ and t are known [52].

Using this model, an effective 480 nm absorption cross-section of $(1.3 \pm 0.35) \times 10^{-16}$ cm^2 and collisional cooling rate constant of $(2.8 \pm 1.6) \times 10^{-11}$ cm^3 molecule^{-1} s^{-1} are calculated from the pressure dependence data shown in Fig. 5. The equivalent effective molar extinction coefficient computed for HBDI$^-$ at 480 nm is $(77{,}000 \pm 21{,}000)$ M^{-1} cm^{-1}. This is in reasonable agreement with the molar extinction coefficient of EGFP at the band maximum (53,000 M^{-1} cm^{-1}) [8]. The effective 480 nm absorption cross-section estimated using this model should somewhat overestimate the true absorption cross section because the model assumes all dissociation results from two-photon excitation whereas the laser power, pressure and pulse rate experiments all point to a single-photon *ePD* component in the photodissociation of HBDI$^-$ at λ_{ex} = 480 nm.

The rate constant for collisional cooling was determined from the Stern–Volmer analysis to be 3×10^{-11} cm^3 molecule^{-1} s^{-1} for helium pressures in the range 0.30–1.92 $\times 10^{-3}$ mbar. This is in good agreement with collisional cooling rate constants for leucine enkephalin in a QIT measured using two-pulse infrared multiple-photon dissociation (IRMPD) by Glish and coworkers [58].

Although the two-photon dissociation model from Dunbar cannot, strictly speaking, be used in the case of HBDI$^-$, where *ePD* takes place, it does allow us to extract a collision rate and absorption cross-sections that are in the expected orders of magnitude. A formal resolution of the set of coupled differential equations underlying our proposed Scheme 2 is, however, required to extract more accurate estimates for these quantities.

4.4. Interpretation of the action spectrum

Finally, we return to the interpretation of the action spectrum of HBDI$^-$ shown in Fig. 2. Unfortunately, the low ion density present in our experimental set-up precludes direct measurement of an absorption spectrum. An action spectrum represents the product of the linear absorption spectrum with the probability of the action (i.e., the quantum yield for *ePD* or probability of subsequent photon absorption and fragmentation) at each wavelength. Zenobi and coworkers [44] have suggested that the gas-phase absorption maximum lies significantly higher in energy than the 480 nm band observed in the QIT and ELISA action spectra and furthermore suggested that the band at 480 nm could be due to an experimental artifact. To support the latter suggestion, two scenarios were advanced [44], neither of which applies to the QIT experimental conditions. The first scenario evoked multi-photon absorption (i.e., absorption of a 2nd photon within the excited state lifetime); as discussed in Section 3.4, the laser pulse rate experiments rule out this possibility with the low pulse energy (50 pJ/pulse) used when constructing the action spectrum in the QIT. The second scenario attributes the 480 nm band to absorption from a vibrationally hot state (a hot band). However, to populate such a vibrationally hot state, absorption of a first photon is invoked. Is the absorption of this first photon not a resonant absorption? Furthermore, for scenario #2 to take effect, the authors refer to "the absence of efficient collisional cooling in ultra-high vacuum" [44] which is clearly not applicable in a quadrupole ion trap ($P_{He} = 2 \times 10^{-3}$ mbar in the QIT action spectroscopy).

Indeed, it is likely the intensity of the feature at 480 nm relative to that of the 450 nm feature is suppressed in the QIT action spectrum in comparison to a linear absorption spectrum. A significant portion of the intensity of the 480 nm peak in the action spectrum arises only from the absorption of multiple photons. Qualitatively, the relative intensity of a process requiring the absorption of multiple photons should be *under-represented* in an action spectrum compared to one-photon processes. The extent of under-representation depends on ion activation rates (i.e., laser power) and deactivation rates (which depends on pressure in the QIT). The latter is significant in the quadrupole ion trap. The lifetime of gaseous HBDI$^-$ upon 480 nm excitation is estimated to be ~200 μs from experiments at ELISA [32]. In comparison, collisions with the helium bath gas in the QIT occur every ~15 μs in the action spectroscopy experiment, resulting in a high probability that photoexcited ions will be collisionally cooled rather than fragment. The discrimination against the 480 nm band in the QIT is further compounded because the lifetime of the dissociating state depends on internal energy of the molecule, which is lower upon absorption of a 480 nm photon compared to a 450 nm photon. Storage ring measurements indicate that the lifetime of the fragmenting state upon excitation in the lower energy 480 nm band (~200 μs) is about 4-fold longer than that at 450 nm (~45 μs) [32]. Thus, the likelihood that a molecule excited at 480 nm will be collisionally deactivated without fragmentation is significantly higher than that for a molecule excited at 450 nm.

A reasonable question is whether the 480 nm feature in the *ePD* action spectrum (green trace, Fig. 2) could be an artifact resulting from *ePD* of fragment ions. MS^3 experiments suggest that this is not the case. MS^3 experiments, in which the m/z 200 fragment ion was formed using collision-induced dissociation, isolated and subsequently irradiated, show that extremely high powers are necessary to photodissociate the m/z 200 fragment to a significant extent (Supplementary Information). Using the same low power and short time used to construct the action spectrum, only ~2% of the m/z 200 fragment undergoes *ePD*, suggesting that this process is negligible. Of course, we cannot rule out the possibility that *ePD* occurs from hot fragment ions (distinct from those formed by CID), though it seems likely that *ePD* occurs from an electronically excited state while loss of methyl (thus forming m/z 200) can occur in the ground electronic state. An alternative explanation for the similarity of shape of the *ePD* and photofragmentation action spectra at 480 nm is that, at this wavelength, *ePD* and fragmentation go through a common intermediate. In other words, absorption occurs transferring the molecule to a common excited state (HBDI$^{-\dagger^*}$ in Scheme 2) which then partitions to follow either the electron detachment or fragmentation pathway.

What then is the relative magnitude of the absorption cross section of 480 nm versus 450 nm photons? One route to answer this question is to examine the difference between 480 nm effective absorption cross section (Section 4.3) and 410 nm *ePD* cross section (Section 4.2); as estimated above, the 480 nm cross section is larger

than the 410 nm cross section by ~70 fold. However, the extracted 480 nm effective absorption cross section is likely an overestimate of the true absorption cross section because, as explained above, the model used to extract this value attributed all dissociation to the absorption of two photons. In contrast, under the experimental conditions used to measure the QIT action spectrum, we can estimate that ~70% of the intensity in the 480 peak is due to 2-photon absorption by using the fitted rate constants (Table 3) to the simplified kinetic model (Eqs. (6)–(10)) and 4 mW irradiation power. In contrast, the *ePD* cross section at 410 nm estimated in Section 4.2 is *lower* than the absorption cross section because the quantum yield of *ePD* is less than one. Unfortunately, we have no estimate for the efficiency of the *ePD* process. If absorption directly accesses the photodetachment continuum, as suggested by the computational work of Epifanovsky et al. [40], this would suggest that the quantum yield of *ePD* is quite high. However, from the experiments we can only deduce an upper bound on the quantum yield of *ePD* of 0.79 at 410 nm. Thus, we can say with certainty that the 70-fold difference in calculated cross section between 480 nm and 410 nm is an overestimate of the true difference in absorption cross section. As a final note, we suggest that the vibronic structure QIT action spectrum measured under the experimental conditions selected may be (somewhat fortuitously, with the possibility for multiple-photon absorptions balanced by collisional cooling rates) close to the linear absorption spectrum. The QIT action spectrum is strikingly similar to both the re-measured ELISA action spectrum [59], which is measured using single-pulse driven photofragmentation under ultra-high vacuum conditions, and to computed vibronic spectra [35,43] (though with origin shifted between the experimental and computed spectra).

5. Conclusions

The photodissociation of the anionic GFP model chromophore ($HBDI^-$) has been investigated in a quadrupole ion trap mass spectrometer at two characteristic wavelengths: 410 nm at which electron detachment is the major deactivation pathway, and 480 nm at which *ePD* and fragmentation both occur. The product yields and branching ratio between photofragmentation and *ePD* is found to be highly sensitive to the relative rates of ion activation and collisional cooling. This is manifested in dependences on laser power, the pressure of He bath gas and the laser pulse rate.

Together the data presented form a picture in which the dissociation of $HBDI^-$ in the quadrupole ion trap results from a combination of single- and multiple-photon dissociation channels under the experimental conditions used. Electron detachment achieved using higher photon energies is a single photon process, which is consistent with a prompt electron detachment channel. This picture fits well with recent calculations by Krylov and coworkers that point to such a low-lying electron photodetachment continuum [40]. At lower photon energies, the fragmentation channels compete favorably with electron detachment, provided that the rate of two-photon excitation exceeds the rate of collisional cooling. Although multiple photons are not strictly required to stimulate photofragmentation of $HBDI^-$ (*vide* ELISA experiments) [32] the relatively high rates of collisional deactivation in the quadrupole ion trap due to the elevated pressure of helium bath gas dictate that significant yields of fragment ions are observed only in the two-photon regime. Electron detachment yields upon irradiation at 480 nm appear to arise from both single and multiple photon processes. This study contributes to a better understanding of the dissociation mechanisms of $HBDI^-$, and permits a more complete interpretation of the photophysical properties of the GFP chromophore.

Acknowledgments

The HBDI was kindly provided by Prof. Vy Dong (University of Toronto). The authors would like to thank Prof. L.H. Andersen (University of Aarhus) for helpful discussions. Funding for this project was provided by the Canada Foundation for Innovation (CFI), Canada Research Chairs Program, the Natural Sciences and Engineering Research Council (NSERC), the Government of Ontario and the Estate of Margery Warren.

Appendix A. Supplementary data

Supplementary data associated with this article can be found, in the online version, at doi:10.1016/j.ijms.2011.08.016.

References

[1] R.Y. Tsien, The green fluorescent protein, Ann. Rev. Biochem. 67 (1998) 509–544.
[2] T.T. Yang, L.Z. Cheng, S.R. Kain, Optimized codon usage and chromophore mutations provide enhanced sensitivity with the green fluorescent protein, Nucleic Acids Res. 24 (1996) 4592–4593.
[3] M. Ormo, A.B. Cubitt, K. Kallio, L.A. Gross, R.Y. Tsien, S.J. Remington, Crystal structure of the Aequorea victoria green fluorescent protein, Science 273 (1996) 1392–1395.
[4] G. Bublitz, B.A. King, S.G. Boxer, Electronic structure of the chromophore in green fluorescent protein (GFP), J. Am. Chem. Soc. 120 (1998) 9370–9371.
[5] M. Chattoraj, B.A. King, G.U. Bublitz, S.G. Boxer, Ultra-fast excited state dynamics in green fluorescent protein: multiple states and proton transfer, Proc. Natl. Acad. Sci. U.S.A. 93 (1996) 8362–8367.
[6] A.B. Cubitt, R. Heim, S.R. Adams, A.E. Boyd, L.A. Gross, R.Y. Tsien, Understanding, improving and using green fluorescent proteins, Trends Biochem. Sci. 20 (1995) 448–455.
[7] R. Heim, D.C. Prasher, R.Y. Tsien, Wavelength mutations and posttranslational autoxidation of green fluorescent protein, Proc. Natl. Acad. Sci. U.S.A. 91 (1994) 12501–12504.
[8] G.H. Patterson, S.M. Knobel, W.D. Sharif, S.R. Kain, D.W. Piston, Use of the green fluorescent protein and its mutants in quantitative fluorescence microscopy, Biophys. J. 73 (1997) 2782–2790.
[9] A.M. Bogdanov, A.S. Mishin, I.V. Yampolsky, V.V. Belousov, D.M. Chudakov, F.V. Subach, V.V. Verkhusha, S. Lukyanov, K.A. Lukyanov, Green fluorescent proteins are light-induced electron donors, Nat. Chem. Biol. 5 (2009) 459–461.
[10] S. Kojima, H. Ohkawa, T. Hirano, S. Maki, H. Niwa, M. Ohashi, S. Inouye, F.I. Tsuji, Fluorescent properties of model chromophores of tyrosine-66 substituted mutants of Aequorea green fluorescent protein (GFP), Tetrahedron Lett. 39 (1998) 5239–5242.
[11] A.D. Kummer, C. Kompa, H. Niwa, T. Hirano, S. Kojima, M.E. Michel-Beyerle, Viscosity-dependent fluorescence decay of the GFP chromophore in solution due to fast internal conversion, J. Phys. Chem. B 106 (2002) 7554–7559.
[12] K.L. Litvinenko, N.M. Webber, S.R. Meech, Internal conversion in the chromophore of the green fluorescent protein: temperature dependence and isoviscosity analysis, J. Phys. Chem. A 107 (2003) 2616–2623.
[13] D. Mandal, T. Tahara, S.R. Meech, Excited-state dynamics in the green fluorescent protein chromophore, J. Phys. Chem. B 108 (2004) 1102–1108.
[14] H. Niwa, S. Inouye, T. Hirano, T. Matsuno, S. Kojima, M. Kubota, M. Ohashi, F.I. Tsuji, Chemical nature of the light emitter of the Aequorea green fluorescent protein, Proc. Natl. Acad. Sci. U.S.A. 93 (1996) 13617–13622.
[15] K.L. Litvinenko, N.M. Webber, S.R. Meech, An ultrafast polarisation spectroscopy study of internal conversion and orientational relaxation of the chromophore of the green fluorescent protein, Chem. Phys. Lett. 346 (2001) 47–53.
[16] D. Mandal, T. Tahara, N.M. Webber, S.R. Meech, Ultrafast fluorescence of the chromophore of the green fluorescent protein in alcohol solutions, Chem. Phys. Lett. 358 (2002) 495–501.
[17] D. Stoner-Ma, A.A. Jaye, P. Matousek, M. Towrie, S.R. Meech, P.J. Tonge, Observation of excited-state proton transfer in green fluorescent protein using ultrafast vibrational spectroscopy, J. Am. Chem. Soc. 127 (2005) 2864–2865.
[18] N.M. Webber, K.L. Litvinenko, S.R. Meech, Radiationless relaxation in a synthetic analogue of the green fluorescent protein chromophore, J. Phys. Chem. B 105 (2001) 8036–8039.
[19] N.M. Webber, S.R. Meech, Electronic spectroscopy and solvatochromism in the chromophore of GFP and the Y66F mutant, Photochem. Photobiol. Sci. 6 (2007) 976–981.
[20] P.J. Tonge, S.R. Meech, Excited state dynamics in the green fluorescent protein, J. Photochem. Photobiol. A – Chem. 205 (2009) 1–11.
[21] A.F. Bell, X. He, R.M. Wachter, P.J. Tonge, Probing the ground state structure of the green fluorescent protein chromophore using Raman spectroscopy, Biochemistry 39 (2000) 4423–4431.
[22] M. Vengris, I.H.M. van Stokkum, X. He, A.F. Bell, P.J. Tonge, R. van Grondelle, D.S. Larsen, Ultrafast excited and ground-state dynamics of the green fluorescent protein chromophore in solution, J. Phys. Chem. A 108 (2004) 4587–4598.

[23] K.M. Solntsev, O. Poizat, J. Dong, J. Rehault, Y.B. Lou, C. Burda, L.M. Tolbert, Meta and para effects in the ultrafast excited-state dynamics of the green fluorescent protein chromophores, J. Phys. Chem. B 112 (2008) 2700–2711.
[24] S.S. Stavrov, K.M. Solntsev, L.M. Tolbert, D. Huppert, Probing the decay coordinate of the green fluorescent protein: arrest of cis-trans isomerization by the protein significantly narrows the fluorescence spectra, J. Am. Chem. Soc. 128 (2006) 1540–1546.
[25] J. Dong, F. Abulwerdi, A. Baldridge, J. Kowalik, K.M. Solntsev, L.M. Tolbert, Isomerization in fluorescent protein chromophores involves addition/elimination, J. Am. Chem. Soc. 130 (2008) 14096–14097.
[26] J. Dong, K.M. Solntsev, L.M. Tolbert, Solvatochromism of the green fluorescence protein chromophore and its derivatives, J. Am. Chem. Soc. 128 (2006) 12038–12039.
[27] V. Voliani, R. Bizzarri, R. Nifosi, S. Abbruzzetti, E. Grandi, C. Viappiani, F. Beltram, Cis-trans photoisomerization of fluorescent-protein chromophores, J. Phys. Chem. B 112 (2008) 10714–10722.
[28] C.M. Megley, L.A. Dickson, S.L. Maddalo, G.J. Chandler, M. Zimmer, Photophysics and dihedral freedom of the chromophore in yellow, blue, and green fluorescent protein, J. Phys. Chem. B 113 (2009) 302–308.
[29] S.B. Nielsen, A. Lapierre, J.U. Andersen, U.V. Pedersen, S. Tomita, L.H. Andersen, Absorption spectrum of the green fluorescent protein chromophore anion in vacuo, Phys. Rev. Lett. 87 (2001).
[30] L.H. Andersen, A. Lapierre, S.B. Nielsen, I.B. Nielsen, S.U. Pedersen, U.V. Pedersen, S. Tomita, Chromophores of the green fluorescent protein studied in the gas phase, Eur. Phys. J. D 20 (2002) 597–600.
[31] L. Lammich, M.A. Petersen, M.B. Nielsen, L.H. Andersen, The gas-phase absorption spectrum of a neutral GFP model chromophore, Biophys. J. 92 (2007) 201–207.
[32] L.H. Andersen, H. Bluhme, S. Boye, T.J.D. Jorgensen, H. Krogh, I.B. Nielsen, S.B. Nielsen, A. Svendsen, Experimental studies of the photophysics of gas-phase fluorescent protein chromophores, Phys. Chem. Chem. Phys. 6 (2004) 2617–2627.
[33] J. Rajput, D.B. Rahbek, L.H. Andersen, T. Rocha-Rinza, O. Christiansen, K.B. Bravaya, A.V. Erokhin, A.V. Bochenkova, K.M. Solntsev, J. Dong, J. Kowalik, L.M. Tolbert, M.A. Petersen, M.B. Nielsen, Photoabsorption studies of neutral green fluorescent protein model chromophores in vacuo, Phys. Chem. Chem. Phys. 11 (2009) 9996–10002.
[34] M.W. Forbes, R.A. Jockusch, Deactivation pathways of an isolated green fluorescent protein model chromophore studied by electronic action spectroscopy, J. Am. Chem. Soc. 131 (2009) 17038–17039.
[35] M.E. Martin, F. Negri, M. Olivucci, Origin, nature, and fate of the fluorescent state of the green fluorescent protein chromophore at the CASPT2//CASSCF resolution, J. Am. Chem. Soc. 126 (2004) 5452–5464.
[36] S. Olsen, S.C. Smith, Bond selection in the photoisomerization reaction of anionic green fluorescent protein and kindling fluorescent protein chromophore models, J. Am. Chem. Soc. 130 (2008) 8677–8689.
[37] S. Olsen, K. Lamothe, T.J. Martinez, Protonic gating of excited-state twisting and charge localization in GFP chromophores: a mechanistic hypothesis for reversible photoswitching, J. Am. Chem. Soc. 132 (2010) 1192–1193.
[38] S. Olsen, R.H. McKenzie, A diabatic three-state representation of photoisomerization in the green fluorescent protein chromophore, J. Chem. Phys. 130 (2009).
[39] E. Epifanovsky, I. Polyakov, B. Grigorenko, A. Nemukhin, A.I. Krylov, The effect of oxidation on the electronic structure of the green fluorescent protein chromophore, J. Chem. Phys. 132 (2010).
[40] E. Epifanovsky, I. Polyakov, B. Grigorenko, A. Nemukhin, A.I. Krylov, Quantum chemical benchmark studies of the electronic properties of the green fluorescent protein chromophore. 1. Electronically excited and ionized states of the anionic chromophore in the gas phase, J. Chem. Theory Comput. 5 (2009) 1895–1906.
[41] I. Polyakov, E. Epifanovsky, B. Grigorenko, A.I. Krylov, A. Nemukhin, Quantum chemical benchmark studies of the electronic properties of the green fluorescent protein chromophore: 2. Cis-trans isomerization in water, J. Chem. Theory Comput. 5 (2009) 1907–1914.
[42] C. Filippi, M. Zaccheddu, F. Buda, Absorption spectrum of the green fluorescent protein chromophore: a difficult case for ab initio methods? J. Chem. Theory Comput. 5 (2009) 2074–2087.
[43] E. Kamarchik, A.I. Krylov, Non-condon effects in the one- and two-photon absorption spectra of the green fluorescent protein, J. Phys. Chem. Lett. 2 (2011) 488–492.
[44] K. Chingin, R.M. Balabin, V. Frankevich, K. Barylyuk, R. Nieckarz, P. Sagulenko, R. Zenobi, Absorption of the green fluorescent protein chromophore anion in the gas phase studied by a combination of FTICR mass spectrometry with laser-induced photodissociation spectroscopy, Int. J. Mass Spectrom. (2011), doi:10.1016/j.ijms.2011.1001.1014.
[45] T. Stafforst, U. Diederichsen, Synthesis of alaninyl and N-(2-aminoethyl)glycinyl amino acid derivatives containing the green fluorescent protein chromophore in their side chains for incorporation into peptides and peptide nucleic acids, Eur. J. Org. Chem. (2007) 899–911.
[46] Q. Bian, M.W. Forbes, F.O. Talbot, R.A. Jockusch, Gas-phase fluorescence excitation and emission spectroscopy of mass-selected trapped molecular ions, Phys. Chem. Chem. Phys. 12 (2010) 2590–2598.
[47] M.W. Forbes, F.O. Talbot, R.A. Jockusch, The spectroscopy of ions stored in trapping mass spectrometers, in: R.E. March, J.F.J. Todd (Eds.), Practical Aspects of Trapped Ion Mass Spectrometry, CRC Press, Boca Raton, FL, 2009, pp. 239–290.
[48] R.E. March, An introduction to quadrupole ion trap mass spectrometry, J. Mass Spectrom. 32 (1997) 351–369.
[49] J.U. Andersen, E. Bonderup, K. Hansen, Thermionic emission from clusters, J. Phys. B – Atomic Mol. Opt. Phys. 35 (2002) R1–R30.
[50] U. Boesl, W.J. Knott, Negative ions, mass selection, and photoelectrons, Mass Spectrom. Rev. 17 (1998) 275–305.
[51] E.E.B. Campbell, R.D. Levine, Delayed ionization and fragmentation en route to thermionic emission: statistics and dynamics, Annu. Rev. Phys. Chem. 51 (2000) 65–98.
[52] R.C. Dunbar, E.W. Fu, Ion photodissociation in 2-photon region – spectroscopy and collisional quenching of bromobenzene cations, J. Phys. Chem. 81 (1977) 1531–1536.
[53] R.C. Dunbar, Pulse-rate effects in the photochemistry of gas-phase bromobenzene ions – a study of ion relaxation mechanisms, J. Phys. Chem. 87 (1983) 3105–3108.
[54] R.C. Dunbar, Photodissociation in the ICR ION Trap, in: M.T. Bowers (Ed.), Gas Phase Ion Chemistry, Academic Press Inc., New York, 1984, pp. 129–166.
[55] J.P. Honovich, R.C. Dunbar, T. Lehman, Laser studies of energy relaxation in gas-phase ion photodissociation, J. Phys. Chem. 89 (1985) 2513–2517.
[56] M.W. Forbes, R.A. Jockusch, Electronic action spectroscopy of the GFP model chromophore in a quadrupole ion trap: electron photodetachment vs. photodissociation, in: Proceedings of the 57th ASMS Conference on Mass Spectrometry and Allied Topics, Philadelphia, Pennsylvania, June, 2009.
[57] B.S. Freiser, J.L. Beauchamp, Laser photodissociation of benzene radical cations – evidence for a 2 photon process involving a long lived intermediate, Chem. Phys. Lett. 35 (1975) 35–40.
[58] D.M. Black, A.H. Payne, G.L. Glish, Determination of cooling rates in a quadrupole ion trap, J. Am. Soc. Mass Spectrom. 17 (2006) 932–938.
[59] M.W. Forbes. Optical Spectroscopy of Mass-selected Ions in the Gas Phase (Ph.D. thesis). University of Toronto, 2010.